



HAL
open science

The response of relative humidity to centennial-scale warming over the southeastern Tibetan Plateau inferred from tree-ring width chronologies

Chunming Shi, Valérie Daux, Zongshan Li, Xiuchen Wu, Tianyi Fan, Qian Ma, Xiaoxu Wu, Huaiyu Tian, Matthieu Carré, Duoying Ji, et al.

► To cite this version:

Chunming Shi, Valérie Daux, Zongshan Li, Xiuchen Wu, Tianyi Fan, et al.. The response of relative humidity to centennial-scale warming over the southeastern Tibetan Plateau inferred from tree-ring width chronologies. *Climate Dynamics*, 2018, 51 (9-10), pp.3735-3746. 10.1007/S00382-018-4107-5 . hal-02190448

HAL Id: hal-02190448

<https://hal.science/hal-02190448v1>

Submitted on 29 Nov 2021

HAL is a multi-disciplinary open access archive for the deposit and dissemination of scientific research documents, whether they are published or not. The documents may come from teaching and research institutions in France or abroad, or from public or private research centers.

L'archive ouverte pluridisciplinaire **HAL**, est destinée au dépôt et à la diffusion de documents scientifiques de niveau recherche, publiés ou non, émanant des établissements d'enseignement et de recherche français ou étrangers, des laboratoires publics ou privés.

[Click here to view linked References](#)

1 **The response of relative humidity to centennial-scale warming over the**
2 **southeastern Tibetan Plateau inferred from tree-ring width**
3 **chronologies**

4 Chunming Shi^a, Valérie Daux^{bf}, Zongshan Li^{c*}, Xiuchen Wu^d, Tianyi Fan^a,
5 Qian Ma^a, Xiaoxu Wu^a, Huaiyu Tian^a, Matthieu Carré^e, Duoying Ji^a, Wenli
6 Wang^a, Annette Rinke^{ag}, Wei Gong^{dh}, Yan Liu^a, Yating Chen^a, Valérie
7 Masson-Delmotte^b

8

9 ^aCollege of Global Change and Earth System Science, Joint Center of Global Change and Green China
10 Development, Beijing Normal University, Beijing 100875, China

11 ^bLaboratoire des Sciences du Climat et de l'Environnement (UMR CEA-CNRS-UVSQ 8212, Institut Pierre
12 Simon Laplace, Gif-sur-Yvette, France)

13 ^cState Key Laboratory of Urban and Regional Ecology, Research Center for Eco-Environmental
14 Sciences, Chinese Academy of Sciences, Beijing 100085, China

15 ^dState Key Laboratory of Earth Surface Processes and Resource Ecology, Faculty of Geographical Science,
16 Beijing Normal University, Beijing 100875, China

17 ^eUM2-CNRS-IRD, Institut des Sciences de l'Evolution de Montpellier, Université Montpellier 2, CC065, Pl.
18 Eugène Bataillon, 34095 Montpellier, France

19 ^fUniversité de Versailles - Saint Quentin, Versailles, France

20 ^gAlfred Wegener Institute Helmholtz Centre for Polar and Marine Research, Potsdam, Germany

21 ^hInstitute of Land Surface System and Sustainable Development, Faculty of Geographical Science, Beijing N
22 ormal University, Beijing 100875, China

23

24 **Corresponding author: Zongshan Li**

25 **Email:** zqli_st@rcees.ac.cn; chunming.shi@bnu.edu.cn

26 **Tel:** +86-10- 62849803

27 **Abstract**

28 Understanding the past variability in atmospheric moisture associated
29 with global warming is essential for reducing the uncertainties in climate
30 projections. Such understanding is especially necessary in the Asian
31 monsoon region in the context of increasing anthropogenic forcing. Here,
32 we average four tree-ring width chronologies from the southeastern
33 Tibetan Plateau (TP) over their common intervals and reconstruct the
34 variability in regional relative humidity (RH) from the previous May to the
35 current March over 1751-2005. In contrast to the summer drying associated
36 with centennial-scale warming and the weakening of the Asian summer
37 monsoon, our RH reconstruction shows no significant centennial trend
38 from the 1820s through the 2000s. This absence of a consistent signal is
39 due to the combined effects of contrasting moisture trends during the
40 monsoonal and non-monsoonal seasons, which are controlled by summer
41 monsoon precipitation and local convective precipitation, respectively. The
42 interannual and decadal variability of our RH reconstruction is modulated
43 by El Niño-Southern Oscillation (ENSO) and the Pacific Decadal
44 Oscillation (PDO); however, these links are unstable over time. Two rapid
45 increases in moisture are found to have occurred around the 1820s and
46 1980s; the latter increase caused the variability in RH during the 1980s-
47 2000s to be the largest over the entire reconstruction period.

49 **1 Introduction**

50 Water vapor is the dominant greenhouse gas in the atmosphere and is
51 associated with a significant positive feedback on global warming, which
52 constitutes a key uncertainty in temperature projections (Hall and Manabe
53 1999; Held and Soden 2000; Held and Soden 2006). Both modelling and
54 observational evidence show that global warming has increased
55 atmospheric water vapor (here defined as specific humidity, SH) (Held and
56 Soden 2000; Dai 2006; Sherwood and Meyer 2006), leading to
57 intensification of the global water cycle and precipitation (Huntington
58 2006; Wentz et al. 2007; Zhang et al. 2007; Durack et al. 2012). A fixed
59 relative humidity (RH) is usually assumed when modelling atmospheric
60 SH changes (Held and Soden 2000). However, both instrumental data and
61 Coupled Model Intercomparison Project Phase 5 (CMIP5) projections
62 indicate that the variability in RH will be region-specific under warmer
63 climate conditions (Dai 2006; Sherwood and Meyer 2006; Sherwood et al.
64 2010).

65 RH is an essential factor that modulates local hydrological and
66 radiative processes by determining the degree of cloud cover and
67 convective precipitation, as well as the rate of precipitation (Sherwood et
68 al. 2010). In plant physiological models, RH is also used to approximate
69 the water vapor deficit, a key factor that dominates stomatal conductance,
70 the rate of photosynthesis and net primary production (NPP). The

71 simulated RH changes in response to anthropogenic forcing depend
72 strongly on the horizontal resolution and the ability to resolve moisture
73 transport of the model used (Sherwood et al. 2010). To date, inconsistent
74 model outputs have been obtained, especially over land (Laine et al. 2014),
75 and large discrepancies between models and observations still exist
76 (Sabeerali et al. 2015). During the monsoon season over Asia, increases
77 and decreases in RH in tropical India and southeastern China are projected
78 by CMIP5 models, respectively (Laine et al. 2014). In contrast, on the
79 Tibetan Plateau (TP), especially the southeastern TP, the RH trends
80 projected by the CMIP5 models are quite ambiguous, and robust
81 conclusions cannot be drawn from these model results (Duan et al. 2013;
82 Laine et al. 2014). Instrumental observations show that the rate of warming
83 over the TP is higher than that of the Northern Hemisphere and other
84 regions at the same latitude, and this fast warming is especially pronounced
85 after the 1980s (Qin et al. 2009; Duan and Xiao 2015). This warming trend
86 has resulted in overall increases in RH and specific humidity (SH) on the
87 TP (Kang et al. 2010; Yang et al. 2014). At the centennial scale, the
88 responses of annual RH to the global warming that has occurred since the
89 Industrial Revolution and the earlier warming that has occurred over the
90 TP and the globe as a whole since the 1820s (Shi et al. 2015; Abram et al.
91 2016; Wilson et al. 2016) are still unclear.

92 The short and sparse instrumental observations over the TP are

93 inadequate to capture the variability in RH on multi-decadal to centennial
94 time scales. Therefore, paleoclimate proxies are increasingly used to
95 reconstruct past moisture variability around the world (Chapter 5 in IPCC
96 AR5, WG1, 2013) and Asia (Cook et al. 2010). Reconstructions using
97 snow accumulation, glacial varves and tree-ring $\delta^{18}\text{O}$ values all indicate
98 summer drying trends in the last century. These trends are associated with
99 reductions in precipitation, RH, and cloud cover over the central, southern
100 and southeastern TP (Shi et al. 2012; Liu et al. 2013; An et al. 2014;
101 Wernicke et al. 2015; Wernicke et al. 2017). These results are consistent
102 with the projected weakening of the Asian summer monsoon in response
103 to climate warming (Sabade et al. 2011; Sun and Ding 2011; Xu et al. 2012;
104 Sooraj et al. 2015). However, these centennial drying trends have not been
105 identified in reconstructions of total annual precipitation over the south-
106 central, southwestern and northern TP (Liu et al. 2011; Yang et al. 2014;
107 Liu and Nina 2015). Due to the lack of annual mean moisture
108 reconstructions, our understanding of past moisture variability is still
109 limited over the southeastern TP.

110 Within the southeastern portion of the TP, the radial growth of trees at
111 elevations of 3200-3500 m a.s.l. is controlled by temperature and
112 precipitation (Fan et al. 2009). Parameters that integrate both signals, e.g.,
113 the self-calibrating Palmer Drought Severity Index (scPDSI), are
114 commonly used as reconstruction targets (Fan et al. 2008; Fang et al. 2010;

115 Bi et al. 2015; Li et al. 2017). Therefore, these reconstructions cannot be
116 used to disentangle the variations in temperature and moisture. Moreover,
117 most previous studies have applied conservative detrending methods in
118 processing tree-ring width (TRW) data. Compared with regional curve
119 standardization (RCS), conservative detrending removes both age-related
120 and climatic long-term trends, inherently leading to flat reconstructions
121 without centennial trends (Esper et al. 2003). Thus, tree-ring
122 reconstructions developed using sampling strategies that are designed
123 specifically to target moisture variability and improved detrending
124 methods are needed to understand the history of moisture conditions over
125 the southeastern TP.

126 In this study, we sampled tree rings from 4 sites across the
127 southeastern margin of the TP at elevations lower than those examined by
128 previous studies. Signal-free RCS was applied to remove the non-climate
129 signals and build standard TRW chronologies. This method preserves the
130 signals of long-term climate and simultaneously avoids “end distortion”
131 effects (Melvin and Briffa 2008). The common intervals of the Z-score
132 standardized chronologies are averaged into a regional chronology and
133 calibrated to instrumental RH measurements. Given the robust coherence
134 between this chronology and the instrumental data, a regional RH
135 reconstruction is produced. The RH reconstruction is analysed in terms of
136 trends and regime shifts and compared with reconstructions of RH, the

137 scPDSI and temperature from nearby areas. The effects of large-scale
138 climate variability over the Pacific Ocean on the regional RH are also
139 analysed and discussed.

140 **2 Materials and methods**

141 **2.1 Study area and meteorological data**

142 Our study region is the northwestern Yunnan Province, which is
143 located on the southeastern margin of the Tibetan Plateau and is the frontier
144 of the summer Asian monsoon into the TP. The elevation of the study
145 region ranges from 1000 m to 6740 m a.s.l. (**Fig. 1**). Land surface
146 meteorological data (maximum temperature, precipitation, and RH) were
147 obtained from two weather stations located at Weixi (2326 m a.s.l.) and
148 Gongshan (1583 m a.s.l.) (**Fig. 1**). These stations have been in operation
149 since 1955 and 1958, respectively. The meteorological data recorded at
150 these 2 stations are highly coherent, and the correlation coefficients for
151 annual mean temperature, total precipitation and RH are 0.62, 0.79 and
152 0.83 ($P < 0.001$ for all of these variables), respectively. Therefore, the
153 averages of the data from the two stations are taken to represent the
154 regional meteorological conditions. The regional annual mean temperature
155 and total precipitation are 13°C and 1343 mm respectively (**Fig. 1**). The
156 summer precipitation of this region is dominated by the South Asian
157 summer monsoon and the East Asian summer monsoon (Wang and Linho
158 2002). The scPDSI values covering the period 1958-2005 at the relevant

159 grid points (extending from 27 to 28°N and from 98 to 101°E) within a
160 globally gridded scPDSI database were extracted and averaged (Dai et al.,
161 2004) to assess the effects of drought on tree growth. Regionally averaged
162 specific humidity, monthly mean temperature and precipitation (27-28°N
163 98-101 °E, 1973-2003) on the land surface were extracted from the
164 HadCRU dataset to identify the factors that dominate the variability in SH.
165 The soil moisture (covering the period between 1960 and 2005) at the
166 sampling sites is simulated using the Community Land Model 4.5 (CLM
167 4.5). To determine the connection between tree growth and large-scale
168 modes of climate variability, such as the Pacific Decadal Oscillation (PDO)
169 and El Niño-Southern Oscillation (ENSO), monthly PDO index values
170 based on the NOAA Extended Reconstructed Sea Surface Temperature
171 (ERSST) dataset and HadISST1 NINO3 index values were downloaded
172 from the NOAA website
173 (<http://www.cdc.noaa.gov/data/climateindices/List/>).

174 **2.2 Tree-ring sampling, processing and chronology construction**

175 The tree-ring samples used in this study were extracted from *Tsuga*
176 *dumosa* (D. Don) Eichler growing in the four counties of Xin Zhu (XZ),
177 Fu Gong (FG), Bing Zhong Luo (BZL) and Ta Cheng (TC) at elevations
178 ranging from 2612 to 2966 m a.s.l. (**Table 1**; red circles in **Fig. 1**). All of
179 the sampling sites are remote from human settlements and display no clear
180 evidence of human activity. *Tsuga dumosa* (D. Don) Eichler is the

181 dominant species below an elevation of 3000 m a.s.l. in northwestern
182 Yunnan Province, and it usually grows in cool and shaded regions. At each
183 site, 33–41 adult trees with straight stems and no signs of damage or
184 internal rotting were selected from areas of open canopy. Two cores per
185 tree were taken from opposite sides of the trees using an increment borer
186 with an inner diameter of 5.14 mm. This process was repeated until at least
187 two cores reached the pith of each tree.

188 The core samples were dried in air and polished with progressively
189 finer sandpaper until the rings were clearly visible. Tree-ring width (TRW)
190 data were obtained using a Lintab® system, which has a resolution of 0.01
191 mm, and cross-dated by visual inspection under a microscope. The cross-
192 dating quality was checked using the COFECHA software package
193 (Holmes 1983). Measurements of pairs of cores from the same tree are
194 averaged.

195 To preserve the long-term climate signals, avoid the effects of “trend
196 distortion” and remove non-climatic signals, the signal-free regional curve
197 standardization (SF-RCS) method (Melvin and Briffa 2008) is applied
198 using the Climatic Research Unit Standardization of Tree-ring data
199 (CRUST) software package (Melvin and Briffa 2014a; b). The TRW series
200 from the individual sites are aligned by biological age (with pith offsets
201 estimated for all samples using the concentric circles method). A signal-
202 free iteration procedure is applied to remove the common growth forcing;

203 thus, the curves used to detrend the TRW data are free of climate signals
204 (Melvin and Briffa 2008). The ring measurements after signal-free iteration
205 are divided by the smoothed RCS curve value of the same ring age to create
206 a TRW index. The robust mean of all of the TRW indices from each site is
207 defined as the standard chronology. Portions of chronologies with sample
208 depths of less than five trees are truncated. The linear trends for 1820-2005
209 are calculated for all the chronologies, and the significance levels of the
210 linear regressions are calculated using the F-test. The multidecadal
211 variations in these chronologies are assessed using 30-year loess
212 smoothing.

213 To ensure the spatial representativeness and quality of the
214 reconstruction, only the common intervals of the chronologies are averaged
215 and standardized using Z-scores to produce a regional chronology. The
216 regional chronology is also calculated by pooling all of the tree-ring
217 materials from the four sites; the TRW data are then detrended using SF-
218 RCS, standardized using Z-scores, and compared with the regional
219 chronology derived using the first method.

220 **2.3 Linear relationships between the TRW chronologies and the** 221 **meteorological data**

222 Correlation coefficients between the chronologies and monthly
223 maximum temperatures, the scPDSI, precipitation, soil moisture and RH
224 are calculated using the Dendroclim2002 software package (Biondi and

225 Waikul 2004) to identify the key climate factors that control tree growth
226 over the instrumental period (**Fig. 3**). The correlation is assessed over the
227 season extending from the previous March to the current September within
228 1959-2005 (1960-2005 for soil moisture).

229 **2.4 Regional climate reconstruction and error calculation**

230 A linear calibration model is used to reconstruct the climate proxy
231 (Fritts 1976), and leave-one-out cross-validation is conducted to test the
232 validity of the model (Michaelsen 1988). The reconstruction errors are
233 calculated as follows. The instrumental RH data and the regional
234 chronology are randomly divided into two halves. Each half is used to
235 calculate a linear calibration model that is validated using the other half,
236 yielding 47 error values. The 2.5% and 97.5% percentiles of the error
237 population after 1,000 iterations are defined as the bounds of the 95%
238 confidence interval of the RH reconstruction.

239 **2.5 Regime shift analysis**

240 To test the shift in the mean value, a regime shift analysis is conducted
241 using a moving window of 30 years in the Regime Shift Detection software
242 package, v3.2 (Rodionov, 2004).

243 **3 Results**

244 **3.1 Chronologies and trends**

245 Principal component analysis of the Z-score standardized TRW
246 chronologies (black lines in **Fig. 2a–d**) shows that the leading principal

247 component explains 47% of the total variance, suggesting a strong
248 common signal among the chronologies. The regional chronologies
249 derived using the two methods described in the Methods section are highly
250 correlated ($R=0.91$, $P<0.001$; black and blue lines in **Fig. 2e**), and the
251 average of the four chronologies is defined as the regional chronology.

252 The TC and FG chronologies show slight but significant ($P<0.05$)
253 increasing and decreasing trends, respectively (**Fig. 2a and 2c**
254 respectively). The BZL and XZ chronologies show no statistically
255 significant trends (**Fig. 2b and 2d** respectively). The 25-year moving
256 expressed population signal (EPS) calculated for each chronology is
257 generally above 0.85 (horizontal red lines in **Fig. 2a-2d**).

258 **3.2 Correlations between TRW chronologies and meteorological data**

259 Monthly maximum temperature shows an overall negative effect on
260 tree growth; however, this effect is insignificant (**Fig. 3a**). The TRW
261 chronologies generally show insignificant correlations with the scPDSI,
262 precipitation and soil moisture in most months (**Fig. 3b, 3c and 3d**).
263 Significant correlation with the scPDSI can only be found in the previous
264 October for BZL and XZ (**Fig. 3b**). Only TC and XZ are significantly
265 correlated with precipitation during the current January (**Fig. 3c**). Despite
266 their statistically insignificant effects on most chronologies, the positive
267 effect of the scPDSI and soil moisture on tree growth is observed for a
268 consecutive period that extends from the previous to the current year (**Fig.**

269 **3b and 3d).**

270 The highest correlation coefficients are obtained between the
271 chronologies and monthly mean RH from the previous May to the current
272 March (pMay-cMar) (**Fig. 3e**). For the regional chronology, the correlation
273 coefficients are significant at the 95% level from pMay to cMar, except for
274 the previous September and November and the current March. The
275 correlation coefficients describing the relationship between the pMay-
276 cMar averaged RH and the individual/regional chronologies fall between
277 0.42 and 0.69, and these correlations are all significant at the 99%
278 confidence level ($R^2=0.48$, $P<0.001$ for the regional chronology) (**Fig. 3e**).

279 **3.3 Regional relative humidity reconstruction**

280 Based on the high correlation coefficients between the regional
281 chronology and the instrumental RH ($R^2=0.48$, $P<0.001$, $n=47$; **Fig. 3e**), a
282 linear calibration model is used to reconstruct the past RH averaged from
283 the previous May to the current March. Specifically, RH_{pMay-}
284 $cMar}=1.55\times\text{chronology}+73.53$ (in %). The values of the reduction of error
285 (RE) statistic and the coefficient of efficiency (CE) and the results of the
286 product means test (PMT) and the sign test (ST) are 0.43, 0.42, 3.36 and
287 12.26 ($P<0.001$), respectively; thus, the linear calibration model is valid
288 for RH reconstruction. Our $RH_{pMay-cMar}$ reconstruction is shown in **Fig. 4**;
289 grey shading indicates the 95% confidence interval. The regime shift
290 analysis demonstrates an abrupt shift towards a wetter state in 1825

291 (significant at the 99% level; thick black line in **Fig. 4**). The trends over
292 1820-2005 and 1850-2005 are statistically insignificant (slope= $-0.0056 \pm$
293 0.02% and $0.0023 \pm 0.003\%$, $P=0.67$ and 0.16 , respectively), and the
294 interannual amplitude is within $\pm 2.55\%$. The greatest decadal variability
295 is noted from the 1980s to the 2000s (red line in **Fig. 4**), and 2004-2005 is
296 the wettest epoch seen in the entire reconstruction period; these features
297 are the results of the rapid increase in $RH_{pMay-cMar}$ since the 1980s.

298 **3.4 Coherence of instrumental and reconstructed RH with PDO and** 299 **ENSO**

300 We calculate the monthly correlation coefficients between the
301 instrumental and reconstructed $RH_{pMay-cMar}$ records with the PDO and
302 ENSO from 1959 to 2005, which is the period that common among all of
303 the climate records except soil moisture (**Fig. 5**). The instrumental and
304 reconstructed $RH_{pMay-cMar}$ are both significantly ($P < 0.05$) and negatively
305 correlated with the PDO index value of the previous year (January-March
306 and February-April, respectively). The instrumental $RH_{pMay-cMar}$ is
307 negatively correlated with the NINO3 index from the previous January to
308 June, but this correlation does not reach the 95% significance level. On the
309 other hand, the $RH_{pMay-cMar}$ reconstruction is significantly and negatively
310 correlated with the NINO3 index from the previous January to April.

311 **4 Discussion**

312 **4.1 Climatic effects on tree growth in the study region**

313 The growth of trees at low elevations generally lack positive
314 temperature signals (Fritts 1976). The mean elevation of our sampling sites
315 is 2738 m a.s.l., which is much lower than those of nearby alpine treelines
316 with elevations of 3522-4221 m a.s.l. (Shi et al. 2015) and is also lower
317 than the nearby sites where a scPDSI reconstruction was obtained (mean
318 elevation 3050 m a.s.l.) (Fang et al. 2010). Thus, our chronologies show
319 insignificant correlation with temperature (**Fig. 3a**). Given that
320 precipitation is abundant (1343 mm/year; **Fig. 1**), the tree growth is
321 unlikely to have been limited by moisture availability, as represented by
322 precipitation, the scPDSI and soil moisture (**Fig. 3b, 3c, 3d**). RH is closely
323 linked with the atmospheric vapor pressure deficit. Low values of RH (i.e.,
324 high vapor pressure deficits) are usually accompanied by low stomatal
325 conductance and even stomatal closure, leading to decreased fluxes of CO₂
326 into leaves and photosynthetic rates (Oren et al. 1999; Flexas and Medrano
327 2002; Lawlor and Cornic 2002). The limiting effect of water vapor deficits
328 on tree growth is prominent for needle-leaf tree species, such as *Pinus*
329 *taeda* and ponderosa pine (Ewers and Oren 2000; Ryan et al. 2000). We
330 suggest that, in this study, the xylogenesis associated with tree growth is
331 limited by the connection between photosynthetic rates and RH.
332 Significant correlations between tree growth and RH in the previous
333 seasons (**Fig. 3e**) and high one-year-lag autocorrelation coefficients (AC1,
334 0.70-0.87) (**Table 1**) have also been reported from nearby regions (Fang et

335 al. 2010). These observations suggest the existence of a “storage” or
336 “memory” effect for this evergreen tree species: photosynthetic products
337 generated prior to the current growing season (including the previous
338 winter) are stored and used for xylogenesis during the following year
339 (Fritts 1976).

340 **4.2 Coherence of the $RH_{pMay-cMar}$ reconstruction and PDO/ENSO at** 341 **interannual to decadal scales**

342 The PDO is a long-lived El Niño-like pattern of climate variability. A
343 robust inverse relationship between the Asian summer monsoon (ASM)
344 and the PDO during the last century has been identified (Krishnan and Sugi
345 2003; Krishnamurthy and Krishnamurthy 2014a). Superimposed on this
346 decadal variability, ENSO also has a significant effect on ASM intensity,
347 mainly at interannual scales (Krishnamurthy and Goswami 2000;
348 Krishnamurthy and Krishnamurthy 2014b). Fang et al. (2010) indicates
349 that the annual mean precipitation and the scPDSI values in a nearby region
350 (blue circles in **Fig. 1**) are modulated by the PDO and ENSO. Similarly,
351 we find significant negative correlations between the instrumental and
352 reconstructed $RH_{pMay-cMar}$ with the PDO and ENSO indices. Both studies
353 confirm that the effects of the PDO and ENSO are not confined to the
354 monsoon season.

355 To test the decadal coherence of $RH_{pMay-cMar}$ and the PDO, both series

356 are smoothed using 30-year loess functions and are shown in **Fig. 6a**.
357 $RH_{pMay-cMar}$ appears to be anti-phased coherent with January-to-April average
358 PDO index values in the post-1960s period (**Fig. 6a**), as is confirmed by
359 wavelet coherence analysis (**Supplementary Fig. 1**). From the 1900s to
360 the 1960s, the coherent pattern appears to be positive (**Fig. 6a**), but wavelet
361 coherence analysis suggests that it is statistically insignificant
362 (**Supplementary Fig. 1**). The correlation and coherence analysis in this
363 study demonstrate that ENSO and the PDO modulate $RH_{pMay-cMar}$ at
364 interannual to decadal time scales. Unstable relationships between
365 PDO/ENSO and moisture variability on the TP have been reported by
366 previous study (Shi et al. 2010).

367 **4.3 Centennial variability in RH and underlying mechanisms**

368 A persistent warming trend since the 1820s has been detected over
369 Asia as a whole (PAGES 2k Consortium 2013). Of the 229 chronologies
370 used in the Asian PAGES 2K project, 98 are from the TP (defined as the
371 region bounded by 27-38°N and 75-103°E). The early onset of global
372 warming from the 1820s has been confirmed by recent studies (Abram et
373 al. 2016; Wilson et al. 2016). Based on seven alpine treeline chronologies,
374 Shi et al. (2014) reported that the summer temperatures in a nearby region
375 (28-33°N 98-103°E) has increased since the 1820s (**Fig. 6b**). The ASM is
376 weakening in response to the centennial-scale warming because the rate of
377 increase in surface temperatures over the subtropical oceans around Asia

378 is faster than that over land, and the land-ocean thermal contrast is
379 decreasing (Sun and Ding 2011; Turner and Annamalai 2012; Xu et al.
380 2012). The weakening ASM and the corresponding decrease in summer
381 RH are evident over the monsoonal TP, i.e., the region between the
382 Tanggula and Himalayan Mountains, as defined by Tian et al. (2001), in
383 the last century (Liu et al. 2013; An et al. 2014; Wernicke et al. 2015;
384 Wernicke et al. 2017). On the other hand, during the non-monsoon season
385 on the southeastern TP, a warm-wet association has been reported for the
386 last several centuries (Li et al. 2017). In the northern (non-monsoonal) TP,
387 where precipitation is controlled by the westerlies, annual precipitation has
388 been found to have increased since the mid-19th century (Yang et al. 2014).
389 Both cases of increased moisture are due to anomalously high evaporation,
390 SH, and local convective precipitation caused by concurrent warming
391 (Yang et al. 2014; Li et al. 2017). The increase in atmospheric SH is the
392 largest positive feedback that drives warming and is the main reason for
393 projections of increased precipitation at middle and high latitudes in model
394 simulations (Dai 2006).

395 In our study region, which receives abundant annual precipitation and
396 displays large variability in the summer monsoon, we assume that different
397 mechanisms that drive SH contribute to the contrasting RH trends in the
398 monsoonal and non-monsoonal seasons. We test this assumption by
399 examining the SH values during the monsoon (June-August, JJA) and non-

400 monsoon seasons (from the previous September to the current May) with
401 the concurrent temperature and precipitation averaged over the sampling
402 region (27-28 °N, 98-101 °E; 1973-2003). The non-monsoonal SH is
403 significantly correlated with the concurrent temperature ($R=0.57$, $P<0.001$;
404 **Fig. 7a**) and does not display a significant correlation with precipitation
405 ($R=0.19$, $P=0.31$; **Fig. 7b**). The abundant precipitation (1343 mm/year)
406 may well have supported the increase in SH with warming during the non-
407 monsoon season over the last several decades, which is an unprecedentedly
408 warm period over the last few centuries (Liang et al. 2009; Liu et al. 2009;
409 Wang et al. 2014; Shi et al. 2015; Wang et al. 2015). In contrast, the SH of
410 the monsoon season is insensitive to temperature variability ($R=0.18$,
411 $P=0.32$; **Fig. 7c**) but is significantly correlated with precipitation amount
412 during the monsoon season ($R=0.56$, $P<0.001$; **Fig. 7d**). The coherence of
413 SH and precipitation during the monsoon season suggests that the summer
414 moisture is controlled by the ASM circulation pattern.

415 RH is usually calculated as the ratio of SH to saturated SH; the latter
416 quantity increases with temperature. Therefore, a temperature-insensitive
417 SH will lead to a minor decrease in RH during the monsoon season
418 (statistically insignificant; black line in **Supplementary Fig. 2**). On the
419 other hand, $RH_{p\text{May-cMar}}$, which is mainly dominated by the non-monsoonal
420 RH (blue and red lines in **Supplementary Fig. 2**), shows a significant
421 increasing trend over the instrumental period; the most prominent tend

422 appears after the 1980s. The opposite trends in RH in the monsoonal and
423 non-monsoonal seasons may represent one reason for the insignificant
424 centennial trend in our $RH_{pMay-cMar}$ reconstruction. However, the interplay
425 of RH between the monsoonal and non-monsoonal seasons over long time
426 scales is still unclear, given that instrumental data are lacking in the past.

427 The long-term increases in CO_2 that have occurred since the Industrial
428 Revolution, particularly the rapid increase in CO_2 over the last decades,
429 could stimulate increased water use efficiency and tree growth of alpine
430 treelines over the southeastern TP since the 1960s (Huang et al. 2017).
431 However, the regional chronology of this study shows no persistent growth
432 enhancement since the 1860s or 1960s (**Fig. 2e**), and the inter-decadal
433 variabilities of the instrumental and reconstructed RH are highly coherent
434 in the last five decades (**Fig. 4**), it seems the CO_2 fertilization effect is
435 insignificant in this study.

436 **4.4 Comparisons with nearby RH and the scPDSI reconstructions**

437 The nearest RH reconstruction, which was published by An et al.
438 (2014) (blue triangle in **Fig. 1**), is compared with our $RH_{pMay-cMar}$ record
439 (**Fig. 6c**). An et al. (2014) showed a persistent decrease in summer RH
440 associated with centennial-scale warming and ASM weakening since the
441 1850s (Liu et al. 2013; An et al. 2014; Wernicke et al. 2015; Wernicke et
442 al. 2017). Our $RH_{pMay-cMar}$ reconstruction lacks long-term trends and
443 represents a combination of opposing moisture trends in the monsoon and

444 non-monsoon seasons with centennial-scale warming. Both our $RH_{pMay-cMar}$
445 record and the RH reconstruction of An et al. (2014) reflect wetting trends
446 in the 1770s through the 1840s (**Fig. 6c**). The abrupt increase in RH_{pMay-}
447 $cMar$ in the 1820s coincides with the onset of significant warming over the
448 southeastern TP (**Fig. 6b**) (Shi et al. 2015), which may have produced
449 increases in SH in the non-monsoon season. In addition, this shift overlaps
450 with a period of elevated summer RH values on the southeastern TP that
451 occurred in the late 1810s. During this period, the ASM was recovering
452 from the previous dry conditions caused by the 1809 Unknown and 1816
453 Tambora volcanic eruptions (Shi et al. 2012). The most strongly
454 contrasting trends between An et al. (2014) and our reconstruction are
455 found in the 1980s-2000s, when an unprecedentedly rapid rate of warming
456 is reported over the southeastern TP (**Fig. 6b**) (Shi et al. 2015). The
457 negative PDO phase and the increased non-monsoon season SH associated
458 with the rapid warming could both have favoured the anomalously high
459 $RH_{pMay-cMar}$ of the last several decades (**Fig. 5, 6a and 7a**)

460 The 30-year smoothing of a nearby scPDSI reconstruction (blue
461 circles in **Fig. 1**; the annually resolved data have not yet been published)
462 that employs a similar seasonal extent (from the previous May to the
463 current April) shows no long-term trend or abrupt regime shift (Fang et al.
464 2010) and is coherent with our $RH_{pMay-cMar}$ reconstruction at the
465 multidecadal scale (**Fig. 6d**). These similarities may arise from a

466 significant correlation between the instrumental annual mean scPDSI and
467 RH values within the sampling region ($R=0.40$, $P=0.004$; 1958-2005).

468 **5 Conclusions**

469 Our results show that atmospheric water vapor on the southeastern TP,
470 specifically the SH during the monsoon and non-monsoon seasons, is
471 controlled by ASM precipitation and local evaporation processes,
472 respectively. Centennial-scale warming has weakened the ASM and
473 decreased summer RH beginning in the mid-19th century on the
474 southeastern TP. Given the abundant precipitation, the warming during the
475 non-monsoon season has increased evaporation and SH. Because our
476 $RH_{pMay-cMar}$ reconstruction represents the combined effects of contrasting
477 moisture trends in the monsoon and non-monsoon seasons, it does not
478 display a centennial trend from the 1820s through the 2000s, when
479 significant warming prevailed over the southeastern TP. Two rapid
480 increases in moisture are detected in the 1820s and 1980s. The former
481 coincides with the onset of significant warming over the southeastern TP
482 and overlaps with the recovery of the ASM from dry conditions caused by
483 consecutive volcano eruptions. The latter is associated with rapid
484 warming and increased SH during the non-monsoon season and may have
485 been additionally enhanced by the negative phase of the PDO.

486

487 **Acknowledgements:** This study was supported by the National Natural
488 Science Foundation of China (NSFC; 31600354), the National Research
489 and Development Programme of China (2016YFC0502105), and the
490 Fundamental Research Funds for the Central Universities.

491 **Table and figure captions:**

492

493 **Tab. 1:** Detailed information on the meteorological stations and sampling sites, as well as summary
494 statistics of the chronologies.

495 **Fig. 1:** Sampling sites and climatic context of the study area.

496 **Fig. 2:** Standardized TRW chronologies and the regional composite of the 4 chronologies.

497 **Fig. 3:** Correlation coefficients between the TRW chronologies and the regional chronology with
498 monthly climate indices.

499 **Fig. 4:** RH reconstruction with regime shift and linear trend analyses.

500 **Fig. 5:** Monthly correlation coefficients of instrumental and reconstructed RH values with the PDO and
501 NINO3 indices.

502 **Fig. 6:** Comparison of our RH reconstruction with the PDO and climate reconstructions from nearby
503 regions.

504 **Fig. 7:** Annual and summer mean SH and temperatures within the sampling region

505 **Supplementary Fig. 1:** Wavelet coherence analysis of RH reconstruction and the PDO.

506

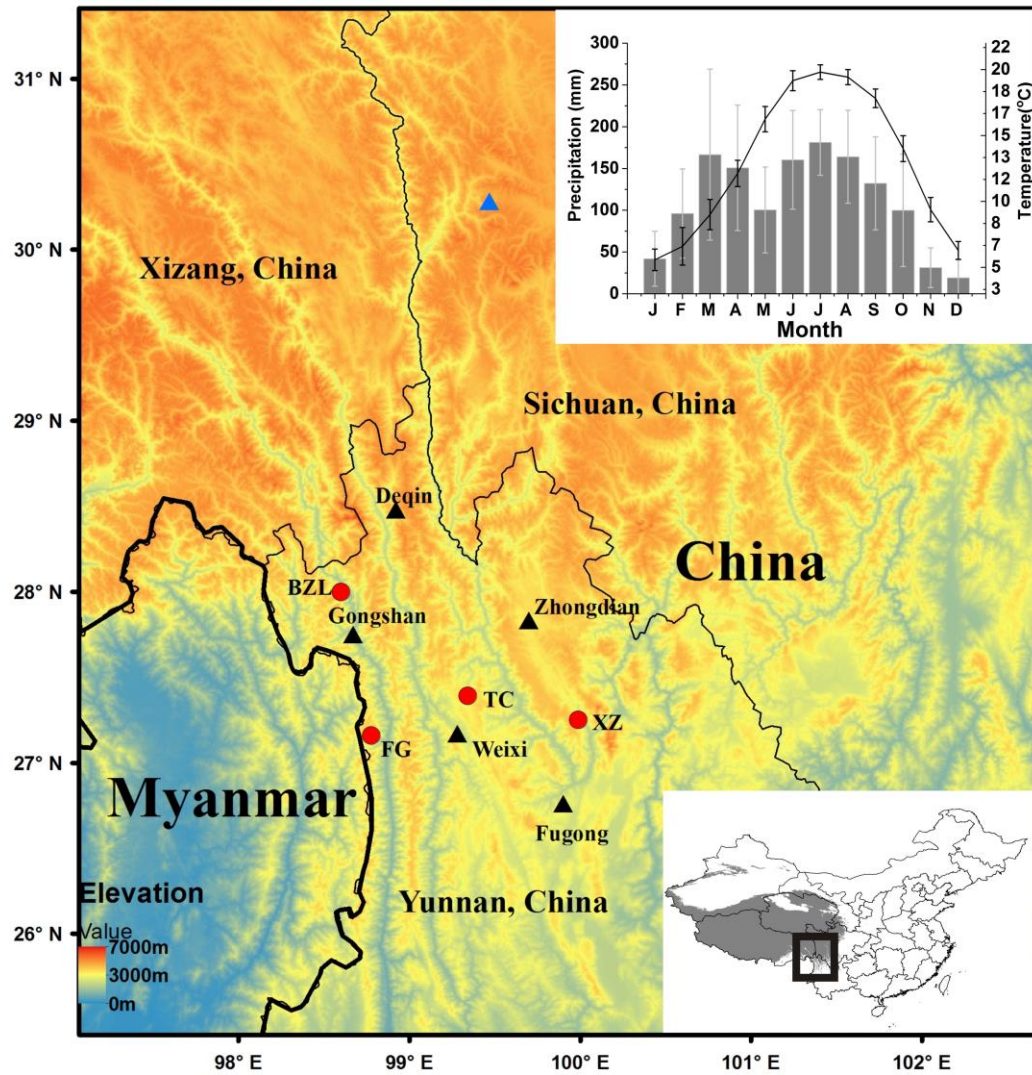
507 **Table 1:** Latitude (Lat. N), longitude (Lon. E) and elevation (Elev.) of the sampling sites, a nearby tree-
508 ring study (Fang et al. 2010) and meteorological stations; the species and number of successfully cross-
509 dated trees at each site (N. tr.); the mean sensitivity (MS) and first order autocorrelation coefficient (AC1)
510 of the chronologies; and the time spans covered by data from the weather stations and chronologies
511 (Sta./Tr. Span).

512

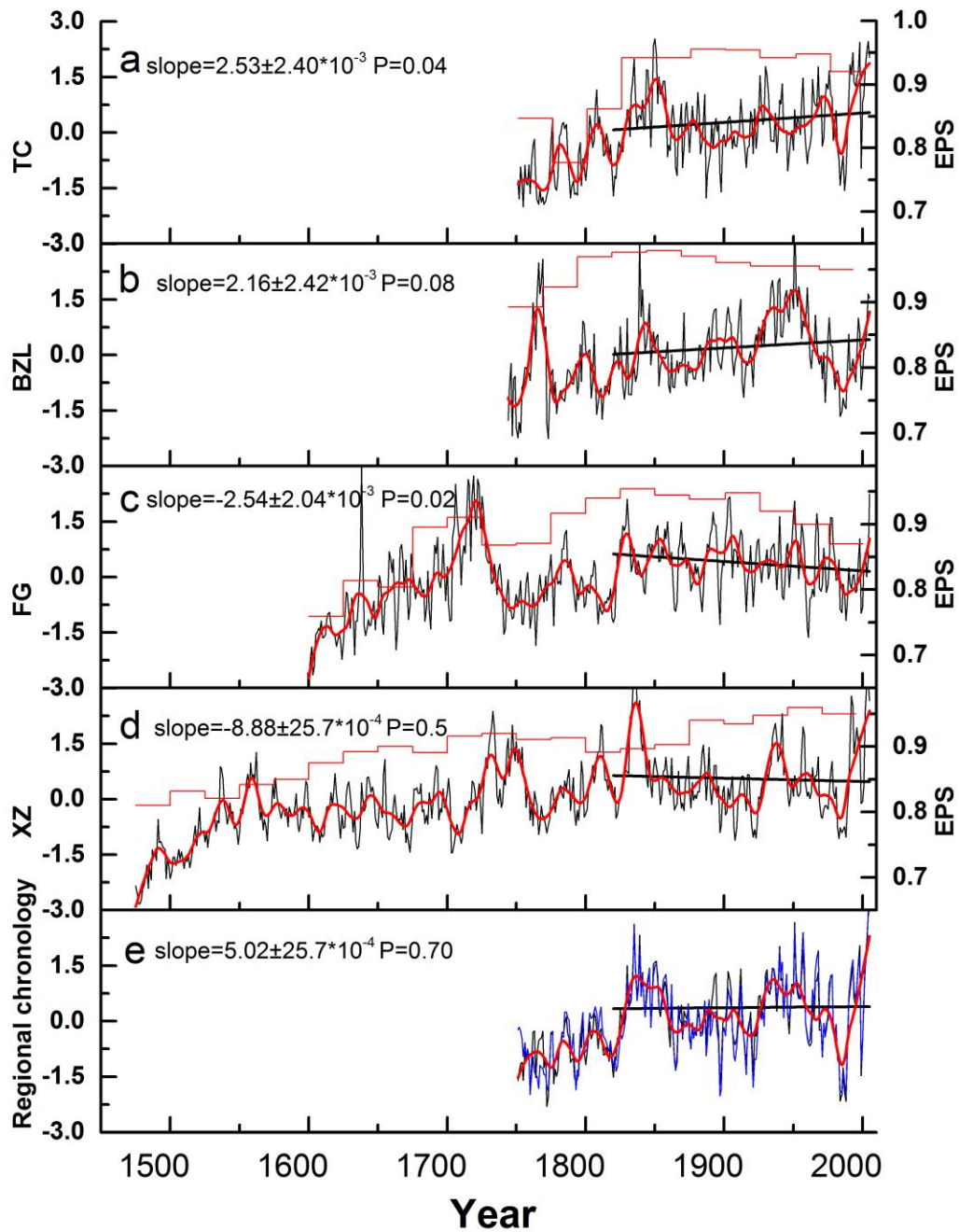
Sites/Stations	Lat. N	Lon. E	Elev. (m)	N. tr.	MS	AC1	Species	Sta./Tr. Span
XZ	27.25	98.99	2966	41		0.87	<i>Tsuga dumosa</i>	1475-2005
FG	26.99	98.82	2731	37		0.77	<i>Tsuga dumosa</i>	1600-2005
BZL	28.00	98.61	2612	33		0.70	<i>Tsuga dumosa</i>	1744-2005
TC	27.39	99.34	2825	36		0.73	<i>Tsuga dumosa</i>	1751-2005
WXI	27.33	99.29	3060	24	0.23	0.85	<i>Abies forrestii</i>	1349-2007
WEX	27.31	99.30	3040	25	0.24	0.83	<i>Abies forrestii</i>	1348-2007
PTG	27.59	99.45	3050	15	0.22	0.82	<i>Abies forrestii</i>	1483-2007
Gongshan	27.45	98.40	1583					1958-2005
Weixi	27.10	99.17	2326					1955-2005

513

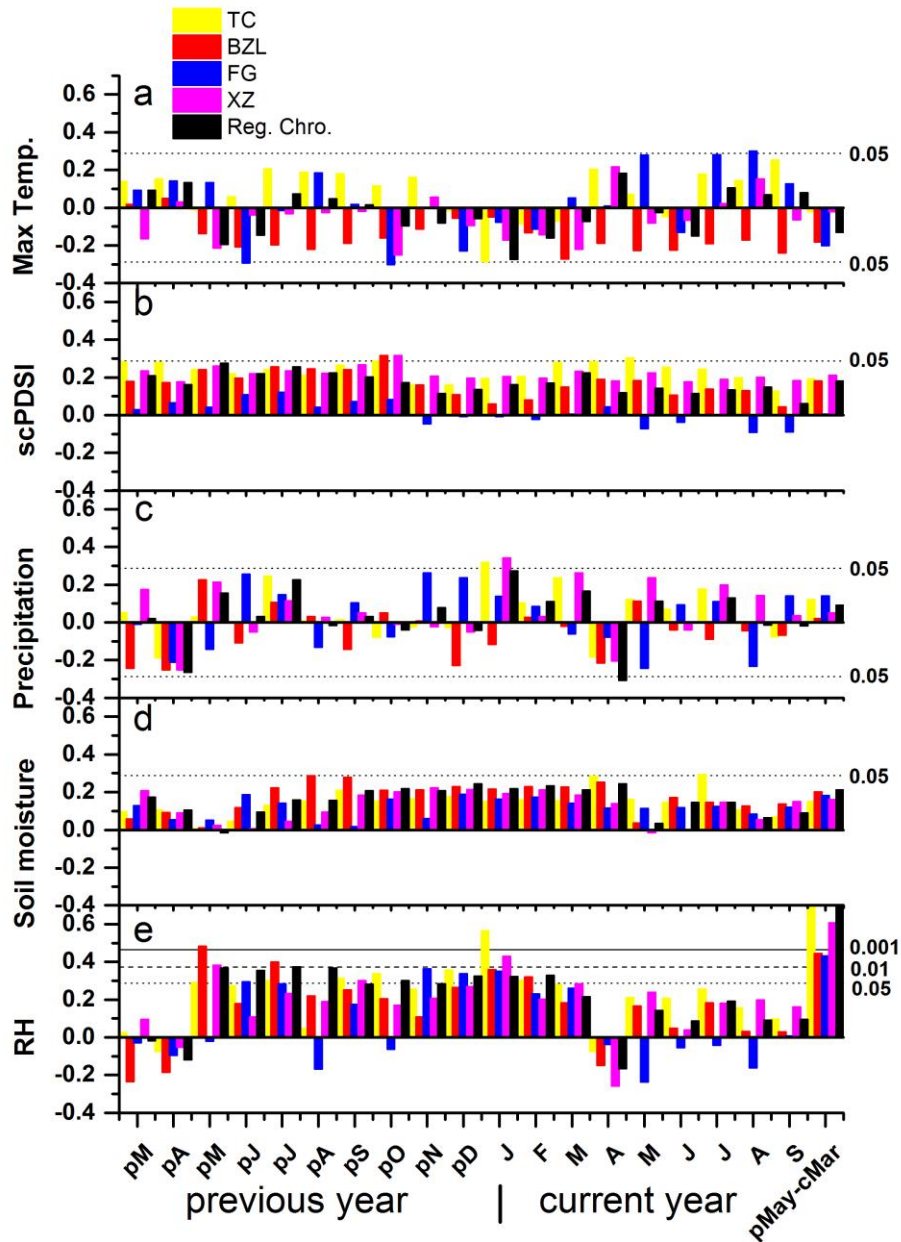
514 **Figure 1:** Sampling sites and study area. The right bottom insert shows the TP (grey shading indicates
 515 elevations above 3000 m) and the sampling region (black rectangle). The right top inset displays a Walter-
 516 Lieth diagram of the study region; the temperatures (black curve) and precipitation (grey bars) represent
 517 the average values from the Weixi and Gongshan meteorological stations (1959-2005). Within the
 518 sampling region (main figure), the filled red circles indicate our sampling sites (see Table 1 for details),
 519 whereas the filled triangles show the positions of nearby meteorological stations. The blue circles and
 520 triangle indicate the sampling sites of nearby reconstructions of the scPDSI and RH (An et al. 2014; Fang
 521 et al. 2010).



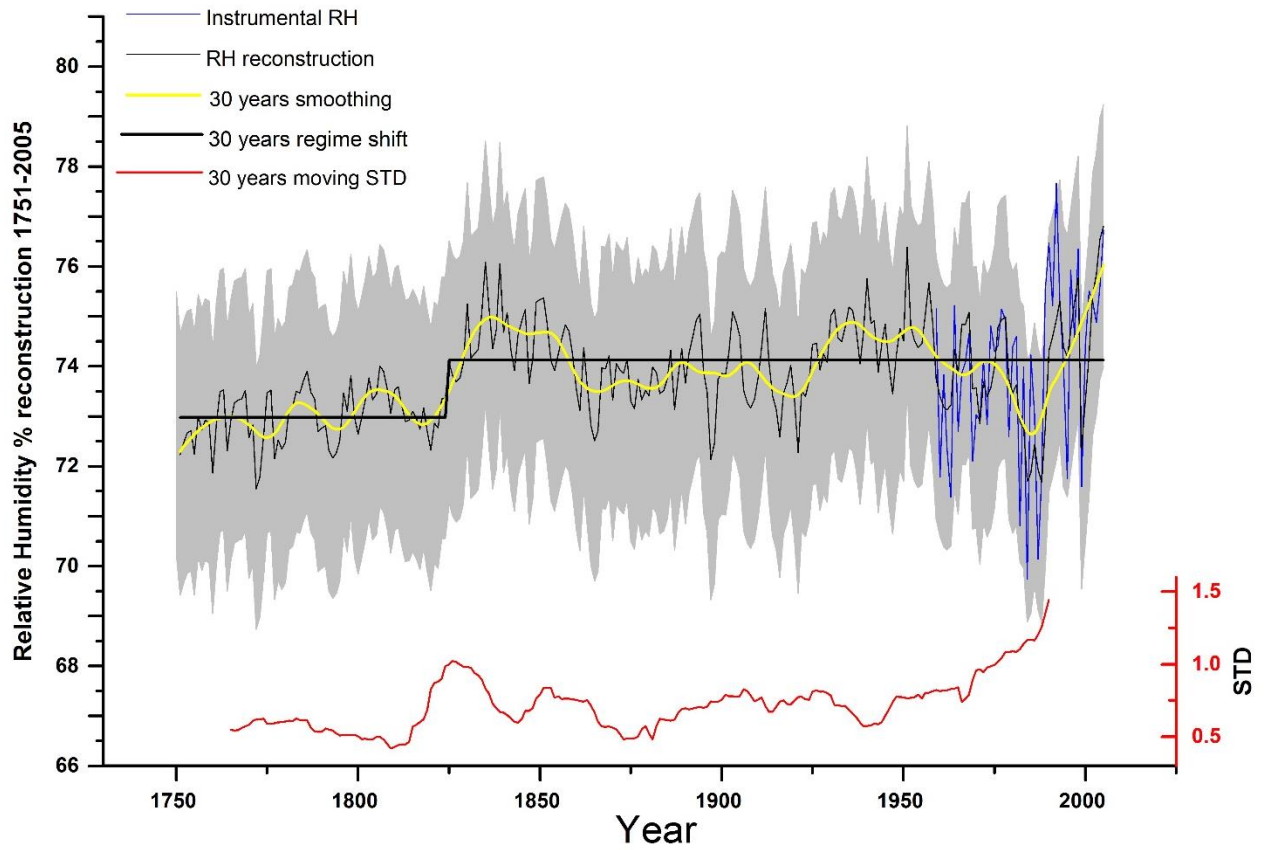
523 **Figure 2:** Z-score standardized TRW chronologies (a-d, SF-RCS detrended) and regional chronologies
 524 derived from the two methods (e). Thick red lines show the 30-year loess-smoothed chronologies. Thick
 525 black lines represent the linear trends calculated for each chronology from 1820 to 2005. Horizontal red
 526 lines represent the 25-year moving expressed population signal (EPS) value for each chronology (right-
 527 hand vertical axis).



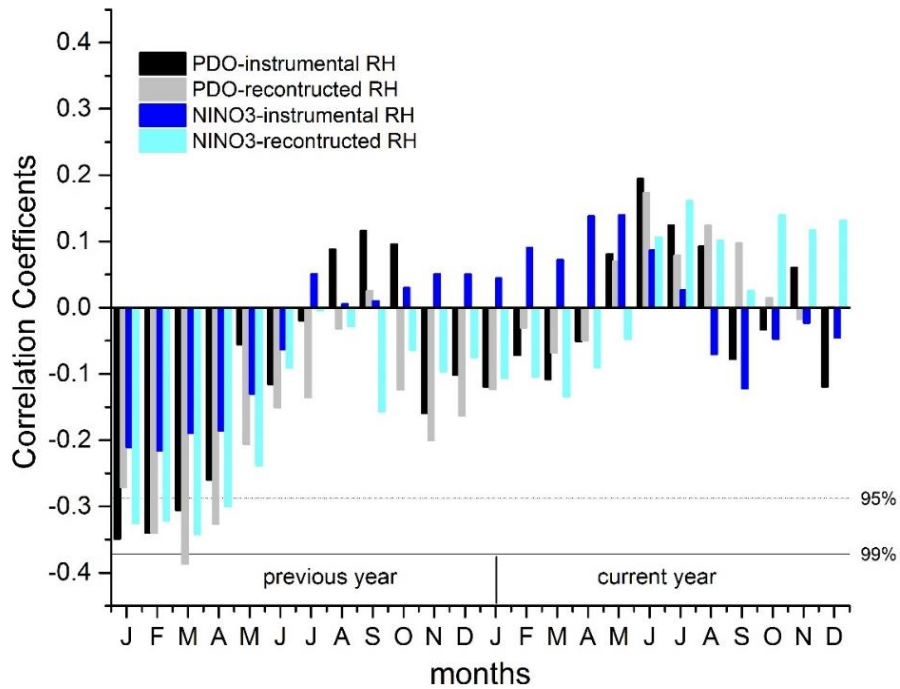
529 **Figure 3:** Correlation coefficients between the TRW chronologies and the regional chronology (Reg.
 530 Chro.) with the monthly regional meteorological data from May of the previous year to September of the
 531 current year. 3a: maximum temperature; 3b: the scPDSI; 3c: precipitation; 3d: soil moisture; 3e: RH.
 532 Correlation coefficients between the TRW chronologies and Reg. Chro. with RH averaged from the
 533 previous May to the current March (pMay-cMarch) are shown in 3e. Significance levels of 0.05, 0.01
 534 and 0.001 are shown as dotted, dashed and solid lines, respectively.
 535



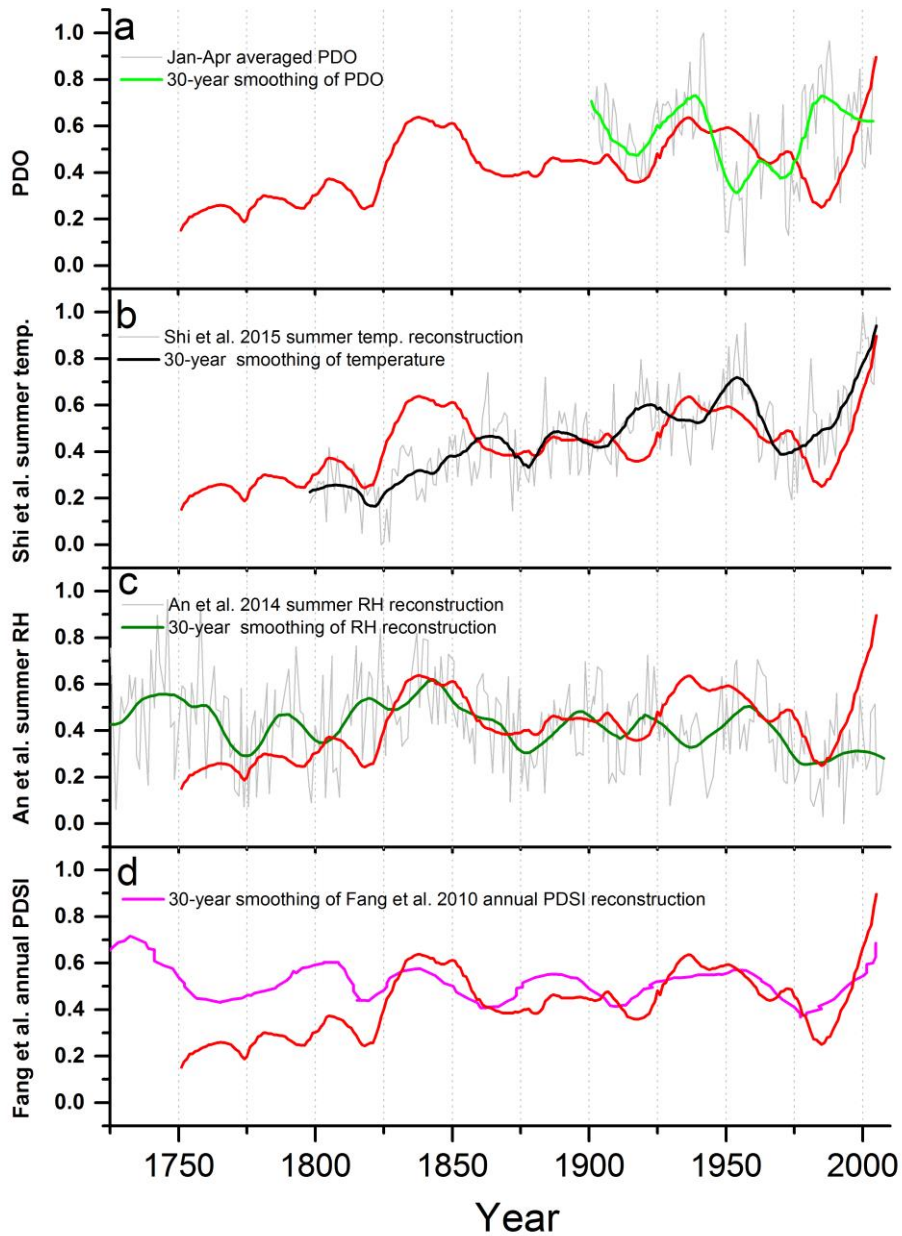
536 **Figure 4:** Relative humidity reconstruction (thin black line) and instrumental RH_{pMay-cMar} (blue line);
537 the 95% confidence interval of the reconstruction is indicated with grey shading. The thick black line
538 shows a shift in the moving mean value (i.e., a regime shift; significant at the 95% level). Red and
539 yellow lines represent the 30-year standard deviation and loess smoothing of the reconstruction,
540 respectively.
541
542



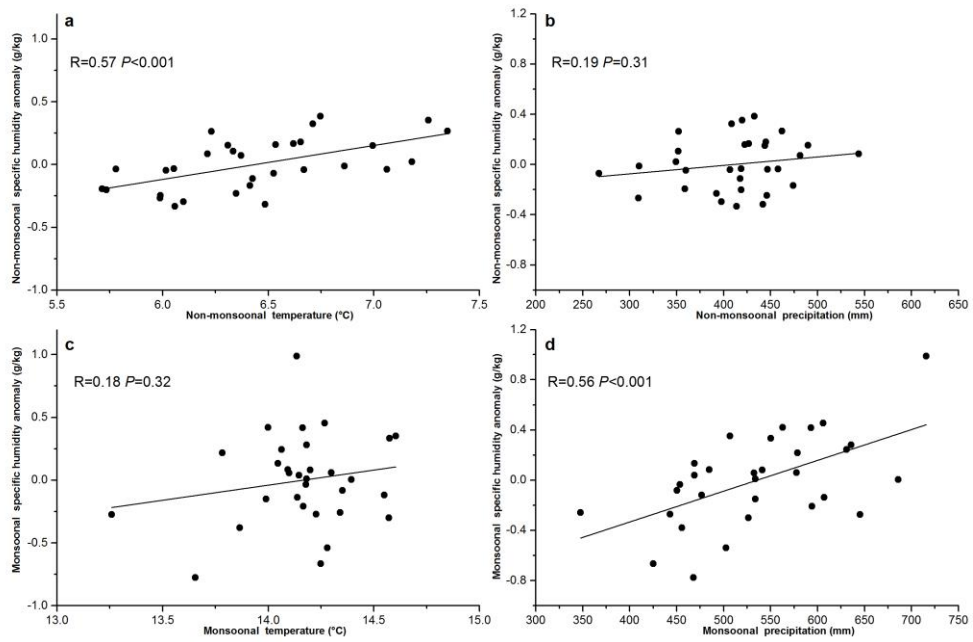
543 **Figure 5:** Monthly correlation coefficients of the instrumental and reconstructed $RH_{pMay-cMar}$ with the
544 PDO and NINO3 indexes from the previous January to the current December. Significance levels of
545 95% and 99% are shown as dotted and solid lines.
546



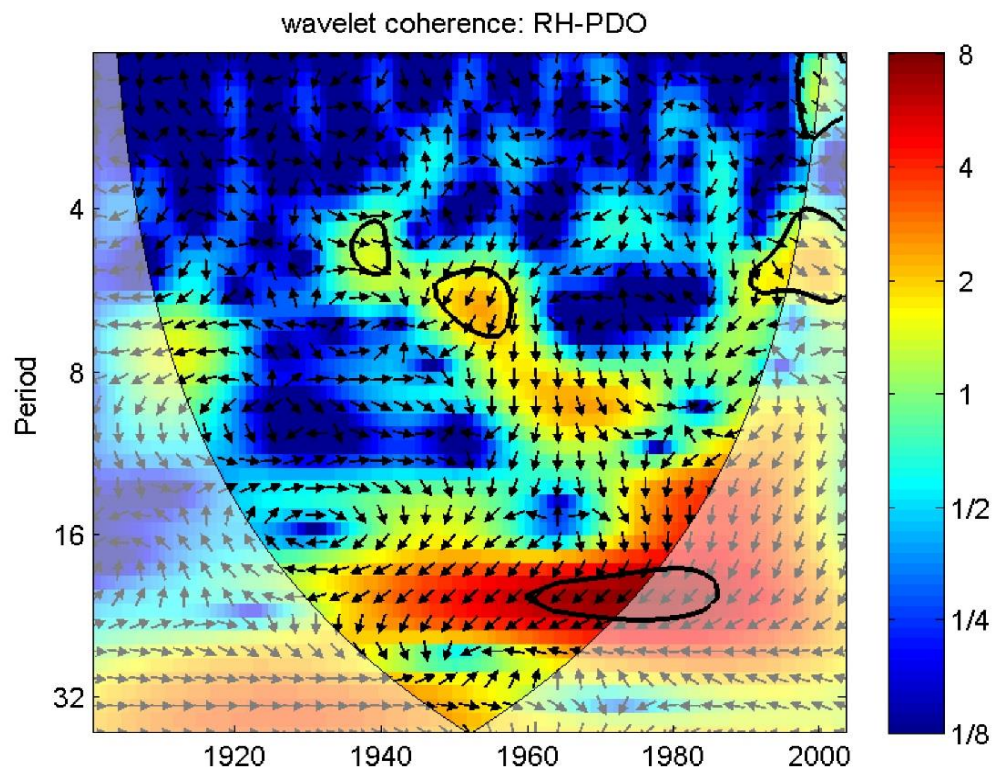
547 **Figure 6:** Comparison of our RH reconstruction (red line) with the PDO index and climate
548 reconstructions from nearby regions. (a): Jan-Apr averaged PDO; (b): regional summer temperature
549 reconstruction (N 28–33° E 98–103°) published by Shi et al. 2015; (c): summer RH reconstruction
550 published by An et al. 2014 (blue triangle in **Fig. 1**); (d): annual scPDSI reconstruction published by
551 Fang et al. 2010 (blue circles in **Fig. 1**). All data are normalized to 0-1 and smoothed with a 30-year loess
552 function.



554 **Figure 7:** Correlation coefficients of the non-monsoonal and monsoonal (JJA) SH with the concurrent
555 temperature and precipitation within the study region.
556

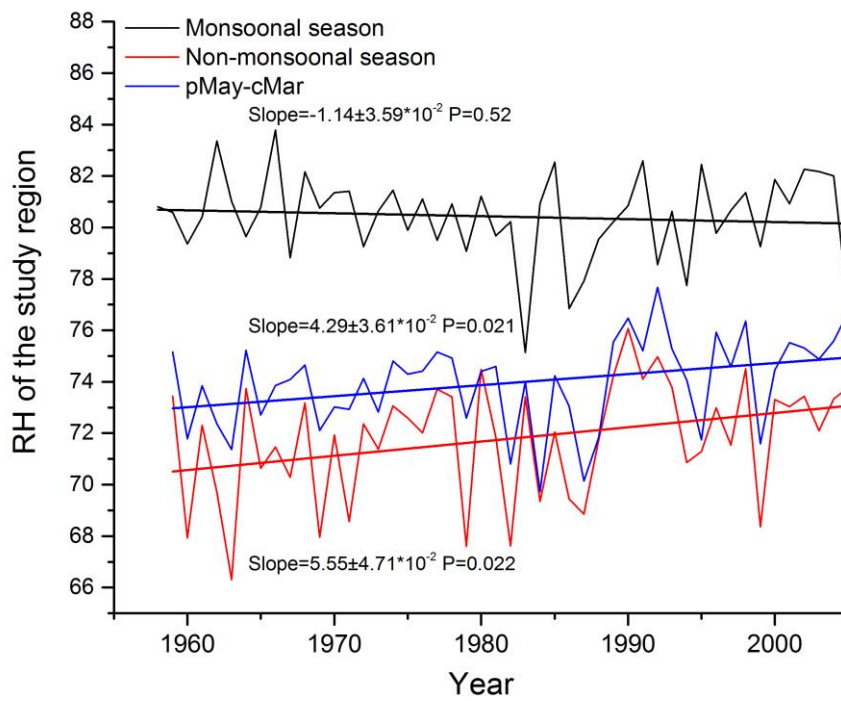


557 **Supplementary Figure 1:** Wavelet coherence analysis of the RH reconstruction and the January-to-
558 April averaged PDO. Black symbols indicate significant coherence at the 95%
559 level.
560
561



562

563 **Supplementary Figure 1:** Regional RH of the study region (average of Weixi and Gongshan stations).
564 Black, blue and red lines indicate the monsoonal, pMay-pMar and non-
565 monsoonal seasons.



References:

567

- 568 Abram NJ, Mcgregor HV, Tierney JE, Evans MN, Mckay NP, Kaufman DS (2016) Early onset of
569 industrial-era warming across the oceans and continents. *Nature* 536: 411
- 570 An W, Liu X, Leavitt SW, Xu G, Zeng X, Wang W, Qin D, Ren J (2014) Relative humidity history on
571 the Batang-Litang Plateau of western China since 1755 reconstructed from tree-ring delta O-18 and
572 delta D. *Clim Dynam* 42: 2639-2654
- 573 Bi Y, Xu J, Gebrekirstos A, Guo L, Zhao M, Liang E, Yang X (2015) Assessing drought variability since
574 1650 AD from tree-rings on the Jade Dragon Snow Mountain, southwest China. *Int J Climatol* 35:
575 4057-4065
- 576 Biondi F, Waikul K (2004) DENDROCLIM2002: A C++ program for statistical calibration of climate
577 signals in tree-ring chronologies. *Comput Geosci-Uk* 30: 303-311
- 578 Cook ER, Anchukaitis KJ, Buckley BM, D'Arrigo RD, Jacoby GC, Wright WE (2010) Asian Monsoon
579 Failure and Megadrought During the Last Millennium. *Science* 328: 486-489
- 580 Dai A (2006) Recent climatology, variability, and trends in global surface humidity. *J Clim* 19: 3589-
581 3606
- 582 Duan A, Hu J, Xiao Z (2013) The Tibetan Plateau Summer Monsoon in the CMIP5 Simulations. *J Clim*
583 26: 7747-7766
- 584 Duan A, Xiao Z (2015) Does the climate warming hiatus exist over the Tibetan Plateau? *Sci Rep-Uk* 5
- 585 Durack PJ, Wijffels SE, Matear RJ (2012) Ocean Salinities Reveal Strong Global Water Cycle
586 Intensification During 1950 to 2000. *Science* 336: 455-458
- 587 Esper J, Cook ER, Krusic PJ, Peters K, Schweingruber FH (2003) Tests of the RCS method for preserving
588 low-frequency variability in long tree-ring chronologies. *Tree-Ring Res* 59: 81-98
- 589 Ewers BE, Oren R (2000) Analyses of assumptions and errors in the calculation of stomatal conductance
590 from sap flux measurements. *Tree Physiol* 20: 579-589
- 591 Fan Z, Brauning A, Cao K (2008) Tree-ring based drought reconstruction in the central Hengduan
592 Mountains region (China) since AD 1655. *Int J Climatol* 28: 1879-1887
- 593 Fan Z, Braeuning A, Cao K, Zhu S (2009) Growth-climate responses of high-elevation conifers in the
594 central Hengduan Mountains, southwestern China. *Forest Ecol Manag* 258: 306-313
- 595 Fang K, Gou X, Chen F, Li J, D'Arrigo R, Cook E, Yang T, Davi N (2010) Reconstructed droughts for
596 the southeastern Tibetan Plateau over the past 568 years and its linkages to the Pacific and Atlantic
597 Ocean climate variability. *Clim Dynam* 35: 577-585
- 598 Flexas J, Medrano H (2002) Drought-inhibition of photosynthesis in C-3 plants: Stomatal and non-
599 stomatal limitations revisited. *Ann Bot-London* 89: 183-189
- 600 Fritts HC (1976) *Tree Rings and Climate*. London, New York and San Francisco: Academic Press
- 601 Hall A, Manabe S (1999) The role of water vapor feedback in unperturbed climate variability and global
602 warming. *J Clim* 12: 2327-2346
- 603 Held IM, Soden BJ (2000) Water vapor feedback and global warming. *Annu Rev Environ Resour* 25:
604 441-475
- 605 Held IM, Soden BJ (2006) Robust responses of the hydrological cycle to global warming. *J Clim* 19:
606 5686-5699
- 607 Huang R, Zhu H, Liu X, Liang E, Griessinger J, Wu G, Li X, Brauning A (2017) Does increasing intrinsic
608 water use efficiency (iWUE) stimulate tree growth at natural alpine timberline on the southeastern
609 Tibetan Plateau? *Global Planet Change* 148: 217-226

610 Huntington TG (2006) Evidence for intensification of the global water cycle: Review and synthesis. *J*
611 *Hydrol* 319: 83-95

612 Krishnamurthy L, Krishnamurthy V (2014a) Decadal scale oscillations and trend in the Indian monsoon
613 rainfall. *Clim Dynam* 43: 319-331

614 Krishnamurthy L, Krishnamurthy V (2014b) Influence of PDO on South Asian summer monsoon and
615 monsoon-ENSO relation. *Clim Dynam* 42: 2397-2410

616 Krishnamurthy V, Goswami BN (2000) Indian monsoon-ENSO relationship on interdecadal timescale.
617 *J Clim* 13: 579-595

618 Krishnan R, Sugi M (2003) Pacific decadal oscillation and variability of the Indian summer monsoon
619 rainfall. *Clim Dynam* 21: 233-242

620 Laine A, Nakamura H, Nishii K, Miyasaka T (2014) A diagnostic study of future evaporation changes
621 projected in CMIP5 climate models. *Clim Dynam* 42: 2745-2761

622 Lawlor DW, Cornic G (2002) Photosynthetic carbon assimilation and associated metabolism in relation
623 to water deficits in higher plants. *Plant Cell Environ* 25: 275-294

624 Li J, Shi J, Zhang DD, Yang B, Fang K, Yue PH (2017) Moisture increase in response to high-altitude
625 warming evidenced by tree-rings on the southeastern Tibetan Plateau. *Clim Dynam* 48: 649-660

626 Liang EY, Shao XM, Xu Y (2009) Tree-ring evidence of recent abnormal warming on the southeast
627 Tibetan Plateau. *Theor Appl Climatol* 98: 9-18

628 Liu J, Yang B, Qin C (2011) Tree-ring based annual precipitation reconstruction since AD 1480 in south
629 central Tibet. *Quatern Int* 236: 75-81

630 Liu J, Nina D (2015) Tree-ring recorded 644-year precipitation variations on the southwestern Tibetan
631 Plateau. *Quatern Sci* 35: 1082-1092

632 Liu X, Zeng X, Leavitt SW, Wang W, An W, Xu G, Sun W, Wang Y, Qin D, Ren J (2013) A 400-year
633 tree-ring delta O-18 chronology for the southeastern Tibetan Plateau: Implications for inferring
634 variations of the regional hydroclimate. *Global Planet Change* 104: 23-33

635 Liu Y, An ZS, Linderholm HW, Chen DL, Song HM, Cai QF, Sun JY, Tian H (2009) Annual
636 temperatures during the last 2485 years in the mid-eastern Tibetan Plateau inferred from tree rings.
637 *Sci China Ser D Earth Sci* 52: 348-359

638 Masson-Delmotte V, Schulz M, Abe-Ouchi A, Beer J, Ganopolski A, González Rouco JF, Jansen E,
639 Lambeck K, Luterbacher J, Naish T, Osborn T, Otto-Bliesner B, Quinn T, Ramesh R, Rojas M, Shao
640 X, Timmermann A (2013) Information from paleoclimate archives. In: Stocker TF, Qin D, Plattner
641 GK, Tignor M, Allen SK, Boschung J, Nauels A, Xia Y, Bex V, Midgley PM (eds) *Climate change*
642 *2013: the physical science basis. Contribution of working group I to the fifth assessment report of the*
643 *intergovernmental panel on climate change. Cambridge University Press, Cambridge*

644 Melvin TM, Briffa KR (2008) A "signal-free" approach to dendroclimatic standardisation.
645 *Dendrochronologia* 26: 71-86

646 Melvin TM, Briffa KR (2014a) CRUST: Software for the implementation of Regional Chronology
647 Standardisation: Part 1. Signal-Free RCS. *Dendrochronologia* 32: 7-20

648 Melvin TM, Briffa KR (2014b) CRUST: Software for the implementation of Regional Chronology
649 Standardisation: Part 2. Further RCS options and recommendations. *Dendrochronologia* 32: 343-356

650 Michaels HJ, Benner B, Hartgerink AP, Lee TD, Rice S, Willson MF, Bertin R (1988) Seed size variation:
651 magnitude, distribution, and ecological correlates. *Evol Ecol* 2: 157-166

652 Oren R, Sperry JS, Katul GG, Pataki DE, Ewers BE, Phillips N, Schafer K (1999) Survey and synthesis
653 of intra- and interspecific variation in stomatal sensitivity to vapour pressure deficit. *Plant Cell*

654 Environ 22: 1515-1526

655 Qin J, Yang K, Liang S, Guo X (2009) The altitudinal dependence of recent rapid warming over the
656 Tibetan Plateau. *Clim Change* 97: 321-327

657 Ryan MG, Bond BJ, Law BE, Hubbard RM, Woodruff D, Cienciala E, Kucera J (2000) Transpiration
658 and whole-tree conductance in ponderosa pine trees of different heights. *Oecologia* 124: 553-560

659 Sabade SS, Kulkarni A, Kripalani RH (2011) Projected changes in South Asian summer monsoon by
660 multi-model global warming experiments. *Theor Appl Climatol* 103: 543-565

661 Sabeerali CT, Rao SA, Dhakate AR, Salunke K, Goswami BN (2015) Why ensemble mean projection
662 of south Asian monsoon rainfall by CMIP5 models is not reliable? *Clim Dynam* 45: 161-174

663 Sherwood SC, Meyer CL (2006) The general circulation and robust relative humidity. *J Clim* 19: 6278-
664 6290

665 Sherwood SC, Ingram W, Tsushima Y, Satoh M, Roberts M, Vidale PL, O'Gorman PA (2010) Relative
666 humidity changes in a warmer climate. *J Geophys Res Atmos*: 115. 10.1029/2009JD012585

667 Shi C, Daux V, Zhang QB, Risi C, Hou SG, Stievenard M, Pierre M, Li Z, Masson-Delmotte V (2012)
668 Reconstruction of southeast Tibetan Plateau summer climate using tree ring delta O-18: moisture
669 variability over the past two centuries. *Clim Past* 8: 205-213

670 Shi C, Masson-Delmotte V, Daux V, Li Z, Carre M, Moore JC (2015) Unprecedented recent warming
671 rate and temperature variability over the east Tibetan Plateau inferred from Alpine treeline
672 dendrochronology. *Clim Dynam* 45: 1367-1380

673 Shi CM, Masson-Delmotte V, Daux V, Li ZS, Zhang QB (2010) An unstable tree-growth response to
674 climate in two 500 year chronologies, North Eastern Qinghai-Tibetan Plateau. *Dendrochronologia* 28:
675 225-237

676 Sooraj KP, Terray P, Mujumdar M (2015) Global warming and the weakening of the Asian summer
677 monsoon circulation: assessments from the CMIP5 models. *Clim Dynam* 45: 233-252

678 Sun Y, Ding Y (2011) Responses of South and East Asian summer monsoons to different land-sea
679 temperature increases under a warming scenario. *Chinese Sci Bull* 56: 2718-2726

680 Turner AG, Annamalai H (2012) Climate change and the South Asian summer monsoon. *Nat Clim*
681 *Change* 2: 587-595

682 Wang J, Yang B, Qin C, Kang S, He M, Wang Z (2014) Tree-ring inferred annual mean temperature
683 variations on the southeastern Tibetan Plateau during the last millennium and their relationships with
684 the Atlantic Multidecadal Oscillation. *Clim Dynam* 43: 627-640

685 Wang J, Yang B, Ljungqvist FC (2015) A Millennial Summer Temperature Reconstruction for the
686 Eastern Tibetan Plateau from Tree-Ring Width. *J Clim* 28: 5289-5304

687 Wentz FJ, Ricciardulli L, Hilburn K, Mears C (2007) How much more rain will global warming bring?
688 *Science* 317: 233-235

689 Wernicke J, Griessinger J, Hochreuther P, Braeuning A (2015) Variability of summer humidity during
690 the past 800 years on the eastern Tibetan Plateau inferred from delta O-18 of tree-ring cellulose. *Clim*
691 *Past* 11: 327-337

692 Wernicke J, Hochreuther P, Griessinger J, Zhu H, Wang L, Braeuning A (2017) Multi-century humidity
693 reconstructions from the southeastern Tibetan Plateau inferred from tree-ring delta O-18. *Global*
694 *Planet Change* 149: 26-35

695 Wilson R, Anchukaitis K, Briffa KR, Buentgen U, Cook E, D'Arrigo R, Davi N, Esper J, Frank D,
696 Gunnarson B, Hegerl G, Helama S, Klesse S, Krusic PJ, Linderholm HW, Myglan V, Osborn TJ,
697 Rydval M, Schneider L, Schurer A, Wiles G, Zhang P, Zorita E (2016) Last millennium northern

698 hemisphere summer temperatures from tree rings: Part I: The long term context. *Quatern Sci Rev* 134:
699 1-18

700 Xu H, Hong Y, Hong B (2012) Decreasing Asian summer monsoon intensity after 1860 AD in the global
701 warming epoch. *Clim Dynam* 39: 2079-2088

702 Yang B, Qin C, Wang J, He M, Melvin TM, Osborn TJ, Briffa KR (2014) A 3,500-year tree-ring record
703 of annual precipitation on the northeastern Tibetan Plateau. *P Natl Acad Sci Usa* 111: 2903-2908

704 Zhang X, Zwiers FW, Hegerl GC, Lambert FH, Gillett NP, Solomon S, Stott PA, Nozawa T (2007)
705 Detection of human influence on twentieth-century precipitation trends. *Nature* 448: 461-464